Eur. Phys. J. B **9**, 93–104 (1999)

THE EUROPEAN PHYSICAL JOURNAL B

EDP Sciences

An X-ray scattering study of flow-aligned samples of a lyotropic liquid-crystalline hexagonal phase

M. Impéror-Clerc[a] and P. Davidson

Laboratoire de Physique des Solides[b], Bâtiment 510, Université Paris Sud, 91405 Orsay Cedex, France

Received 15 July 1998 and Received in final form 29 October 1998

Abstract. Large flow-aligned samples of the hexagonal mesophase of the (sodium dodecylsulfate, pentanol, water) ternary system were produced by merely sucking the material into flat glass capillaries. These samples were examined by polarized light microscopy and X-ray scattering. In the plane of the hexagonal lattice, the "ϕ–mosaic" is only $\cong 0.1^\circ$ because the dense (10) hexagonal planes lie parallel to the flat glass plates of the capillaries. In contrast, the "χ–mosaic" of the C_6 axis reaches 5–10° because the samples undergo a thermomechanical instability of the columns already investigated by Oswald *et al.* in detail on the ($C_{12}EO_6$, H_2O) system. Anisotropic thermal diffuse scattering is observed around the Bragg peaks and its description in the frame of an elastic continuum model provides estimates of the elastic constants. On heating the samples, we observed a clear splitting of four of the (10) hexagonal lattice reflections. This splitting is the defining signature of the thermomechanical instability by which the columns form zig-zags. The fact that two of the (10) reflections are not affected by the instability demonstrates that it is confined to the plane of the capillary. The influence of temperature on the thermomechanical instability was also studied in detail.

PACS. 61.10.Eq X-ray scattering (including small-angle scattering) – 61.30.-v Liquid crystals – 61.30.Jf Defects in liquid crystals – 65.70.+y Thermal expansion and density changes; thermomechanical effects

1 Introduction

Mesophases of hexagonal symmetry are very often encountered in the field of complex fluids. A large number of molecular moieties or aggregates such as disc-like molecules [1], block-copolymers [2], rod-like polymers [3] and micelles of amphiphilic molecules [4] form a hexagonal mesophase in a given range of concentration and temperature. The hexagonal phase has long-range orientational order but only 2-dimensional long-range positional order [5]. Therefore, there are no long-range positional correlations along the C_6 axis so that the phase only shows a 2-d lattice of Bragg reflections by X-ray scattering. Although there have been numerous structural studies of hexagonal mesophases performed on "powder" samples, only very few aligned samples have been described in the literature. Some hexagonal mesophases spontaneously grow into single domains or may be oriented by a magnetic field [6] but these are rather exceptional cases. Sophisticated techniques such as "strand pulling" [7], the "X-ray Surface Force Apparatus" [8] or shear cells [9] have already been successfully applied to produce aligned samples but simpler methods are clearly needed in order to easily investigate a larger number of hexagonal mesophases. Single domains are very useful for structural studies since very valuable information is lost in the process of powder averaging and the signal-to-noise ratio of a single domain is always much larger than that of a powder. In addition, the study of the thermal diffuse scattering (TDS), which gives access to the elastic constants, requires the use of a single domain. Since the elastic constants are themselves derived from the free energy, the thermal diffuse scattering indirectly gives information on the thermodynamics of the phase [7c]. Direct mechanical measurements [10] of the elastic constants are often complicated by the presence of residual topological defects. In contrast, our approach provides more local estimates which agree well with the values obtained from the analysis of textures [11,12].

In this work, we describe how we produced highly aligned samples of a lyotropic hexagonal mesophase of amphiphilic molecules by merely sucking the material into flat glass capillaries. The molecules form very long cylindrical micelles which are aligned along the capillary main axis by the flow. We characterized these samples by polarized light optical microscopy and X-ray scattering. The TDS is essentially localized around the Bragg reflections and can be described in the frame of an elastic continuum model thus providing estimates of the elastic constants of

[a] e-mail: `imperor@lps.u-psud.fr`
[b] Laboratoire associé au CNRS.

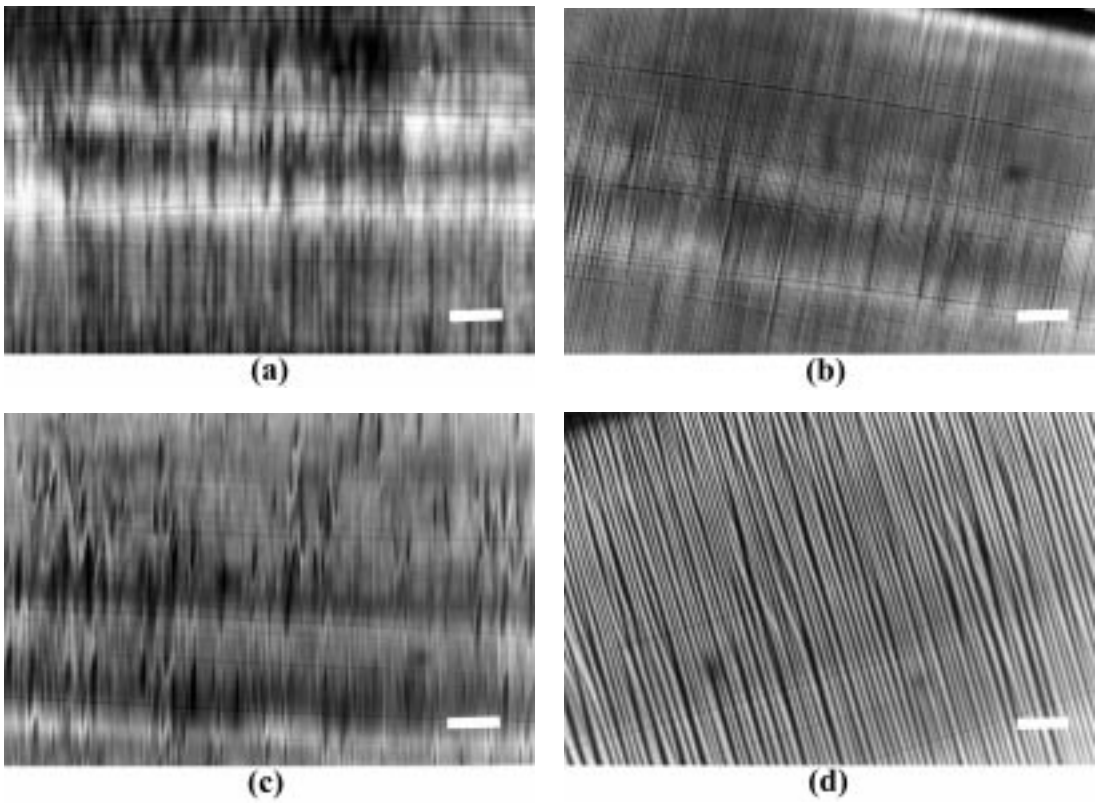

Fig. 1. Textures of the samples in polarized light microscopy (Sample thickness is 100 μm, the white bars are 100 μm long. The crossed polarizers are parallel to the sides of the photographs.) (a) Room temperature, capillary axis parallel to the polarizer direction; (b) Room temperature, capillary axis at an angle $\theta = 5^\circ$ with the polarizer direction; (c) $T = 80\,^\circ$C, capillary axis parallel to the polarizer direction; (d) $T = 80\,^\circ$C, capillary axis at an angle $\theta = 15^\circ$ with the polarizer direction

the hexagonal phase. Besides, we found that the distribution of the TDS is very different from that observed in previous studies of thermotropic hexagonal phases [6a,7c]. Finally, we show that our samples undergo a thermomechanical instability already studied in detail by Oswald *et al.* [12]. This instability reveals itself on heating by the appearance of a striated texture indicative of undulations or zig-zag conformations of the micelles.

2 Experimental

We selected the lyotropic hexagonal phase already reported at room temperature in the ternary phase diagram of sodium dodecylsulfate (SDS), pentanol and water [13]. Homogeneous mixtures of 35.6 w% SDS, 9.2 w% pentanol and 55.2 w% water were prepared by weighing in test-tubes the appropriate amounts of chemicals and mixing them first with a spatula, then with a vortexer. Before use, the test-tubes were left to stand several weeks until the mixtures were completely transparent.

Aligned samples of the hexagonal phase were obtained in flat optical glass capillaries (Vitro Com Inc., Moutain Lakes, NJ, USA), of thicknesses 50 or 100 μm, according to a procedure described in the next section and observed in polarized light with an Olympus BH2 microscope. Textures were photographed using an Olympus camera. The microscope was also equipped with a Mettler heating stage.

Preliminary X-ray scattering experiments were performed in our laboratory using a rotating anode setup (λ CuK$_\alpha$ = 0.154 nm). The X-ray beam delivered by the anode is punctually focused by two perpendicular curved mirrors coated with a 60 nm nickel layer [14]. The mirrors cut the high energy radiations issued from the anode and a 20 μm nickel foil filters the K_β emission line. The X-ray intensity at the sample level is about 10^7 photons/s.mm^2. The scattered X-rays were detected on imaging plates and the sample-detection distance was 50 cm. Exposure times were typically one hour.

Additional high resolution X-ray scattering experiments were performed at the synchrotron beamlines D23 at LURE in Orsay, France and D2AM at ESRF in Grenoble, France. Both beamlines have already been described in detail [15,16] and have very similar designs. The beam is first monochromatized by reflection on a flat Si (111) crystal and then focused in the horizontal plane by reflection on a curved Si (111) crystal. Moreover, the use of mirrors (one for D23 and two for D2AM) ensures the rejection of higher harmonics. On D23, the beam size was (500 μm $\times$ 250 μm) at the sample level and a wavelength of $\lambda = 0.154$ nm was selected. The X-ray beam had a flux of a few 10^9 photons/s.mm^2. The sample was set at the center of a Huber diffractometer equipped with a crystal

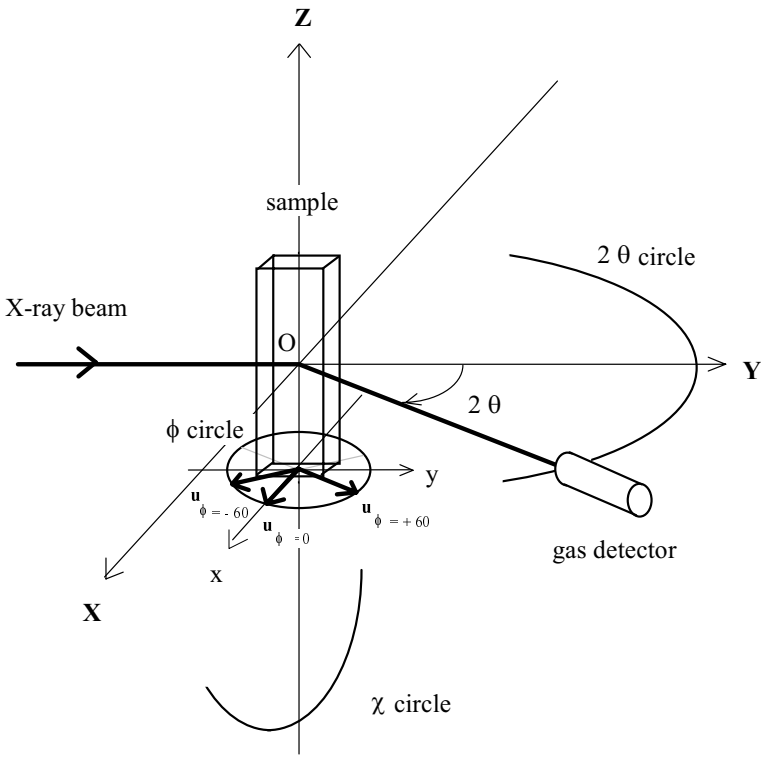

Fig. 2. Schematic drawing of the 4-circle X-ray scattering setup. The gas detector moves along the 2θ-circle in the OXY plane. Its position along the 2θ-circle selects the value of Q. The sample is oriented by using two circles: the χ-circle in the OXZ plane and the ϕ-circle in the OXY plane. The position $\chi = 0$ and $\phi = 0$ corresponds to: (i) The Oz axis of the capillary is parallel to the OZ axis of the diffractometer; (ii) The (10) reticular planes of the 2-d hexagonal lattice lying parallel to the flat plates of the capillary are in reflection position.

analyzer. On D2AM, the beam size was $(250\,\mu\text{m})^2$ at the sample position and a wavelength $\lambda = 0.1549$ nm was selected. The X-ray beam in single bunch mode had a flux of a few 10^{10} photons/s.mm^2. This line is equipped with a "7-circles" diffractometer (Microcontrole, France) which we used in a conventional "4-circles" configuration. On both beamlines, the scattered X-rays were detected either with a Bicron point-detector or using imaging plates fixed onto the analyzer arm. The resolution of the X-ray scans was $\delta Q \cong 7\times10^{-3}$ nm^{-1} (FWHM) with the D23 setup and $\delta Q \cong 1.4\times10^{-2}$ nm^{-1} with the D2AM setup (where $\mathbf{Q}$ is the scattering vector of modulus $Q = (4\pi \sin\theta/\lambda$ and 2θ is the scattering angle). X-ray scans and imaging plate exposures typically required about ten minutes on D23 and two minutes on D2AM. For temperature control, we also used on D2AM a home-made oven and a computer-driven temperature controller.

3 Sample alignment and characterization

Aligned samples were prepared in a very straightforward and reproducible way according to the following procedure. The test tube is first mildly centrifuged upside-down so as to collect all the material at its neck. Meanwhile, the tip of a flat optical glass capillary, of thickness $100\,\mu$m, is connected to a small primary vacuum pump through a rubber hose equipped with a valve. The other tip of the capillary is then dipped into the material and the vacuum pump turned on. The material is thus sucked into the capillary at a speed controlled by the valve. When there is enough material in the capillary, the tip is taken out of the test tube and the material is centered inside the capillary. Usually, the whole process only takes a few seconds. At this point, the vacuum pump can be disconnected and the capillary is flame-sealed at each end.

Immediate inspection of the capillaries by polarized light optical microscopy reveals that the hexagonal phase is highly aligned, in spite of a few defects distributed at random. The capillaries are uniformly bright when their main axis lies at an angle of 45° with respect to those of the polarizer-analyzer system and are dark when they lie parallel to the polarizer-analyzer directions. A more careful examination shows a system of stripes. This system becomes more regular whereas the random defects tend to disappear as the samples anneal over several days (Fig. 1). This procedure takes place at room temperature and obviously will require modifications to be applied to mesophases stable at higher temperatures only.

These samples have been characterized by X-ray diffraction on the LURE D23 beamline in order to fully determine the hexagonal lattice orientation with respect to the capillary axes and the mosaic distributions (Figs. 2 and 3). As inferred from the optical experiments, we

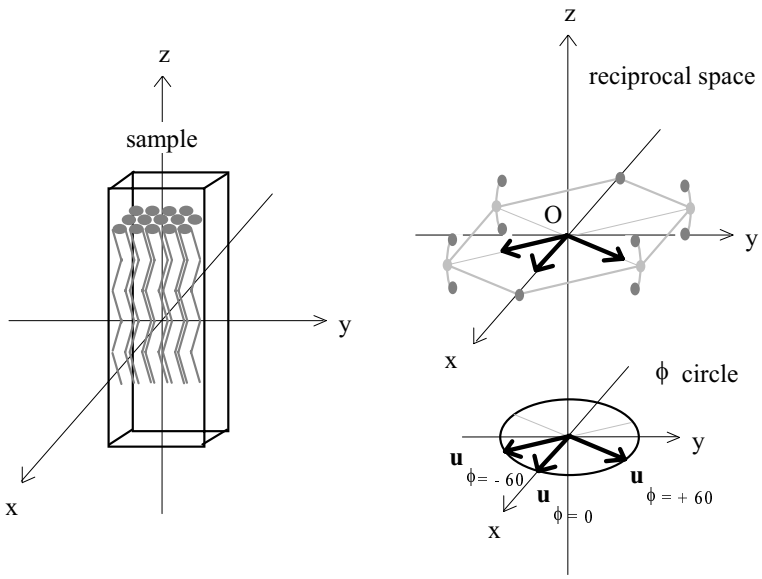

Fig. 3. Diffraction by an aligned sample. The average direction of the columns is along Oz, the direction of the capillary axis. Because of the strong anchoring of a family of (10) reticular planes on the flat walls of the capillary, the direction Ox ($\phi = 0$) corresponds to a Bragg reflection. Two other Bragg reflections are recorded for $\phi = 60°$ and $\phi = -60°$, as expected for a hexagonal C_6 axis along Oz. On heating, the thermomecanical instability is observed in the reciprocal space. Each Bragg spot at $\phi = 60°$ and $\phi = -60°$ splits into two spots, corresponding to the two types of domains of the zig-zag texture. The Bragg spot at $\phi = 0°$ is not affected, showing that the zig-zag texture only develops within the Oyz plane.

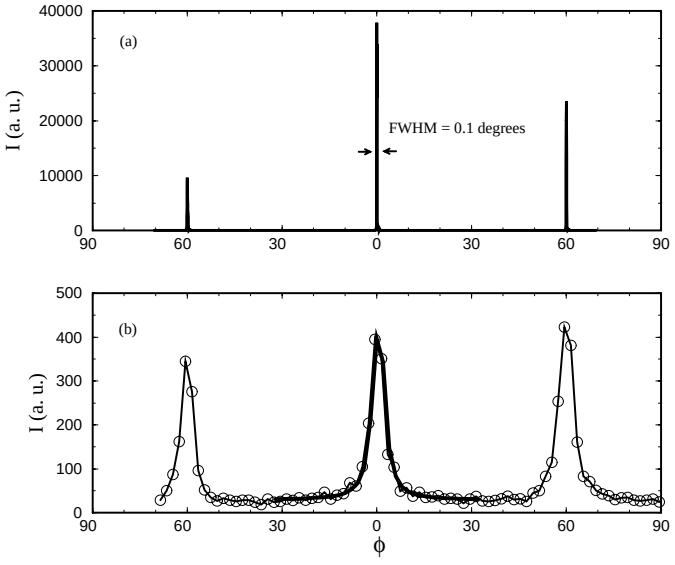

Fig. 4. ϕ-scans at room temperature of an aligned sample. (a) ϕ-scan at $Q = Q_{\mathrm{Bragg}} = 1.542$ nm^{-1}. Three Bragg peaks at $\phi = -60°$, $\phi = 0°$ and $\phi = 60°$ with a FWHM of 0.1° are recorded. The three peaks have different intensities essentially because the OZ diffractometer axis and the Oz sample axis are not perfectly parallel. (b) ϕ-scan at $Q = Q_{\mathrm{Bragg}} + \Delta Q$, with $\Delta Q/Q_{\mathrm{Bragg}} = 2.4\%$. The thermal diffuse scattering signal (see Sect. 4) of each peak is only recorded in this case. The fitted intensity using the continuum elastic model with $\alpha = 2.94$ is shown (thick solid line) for one Bragg spot. Intensity units are the same in (a) and (b).

observe that the C_6 axis is oriented along the capillary main axis Oz. Moreover, we also observe that a family of dense planes (10) of the hexagonal lattice lie parallel to the capillary flat walls. The azimuthal "ϕ-scan" shown in Figure 4a is a scan for which $\mathbf{Q}$ describes a circle, of constant modulus Q_{Bragg}, going through the (10) reflections of the 2-d hexagonal lattice. Three (10) reflections can be seen equally spaced by 60° as expected and no other hexagonal domain can be detected. A more detailed scan allows us to measure the "ϕ-mosaic" (*i.e.* the width of the ϕ distribution for all the crystallites in the X-ray beam), which is found to be 0.1° full width at half maximum (FWHM). The scan presented in Figure 4a is a typical one for samples prepared by this method. Poor samples may show a worse ϕ-mosaic that may reach up to 0.25° or several domains in the beam. Outstanding samples may have a ϕ-mosaic as low as 0.03°, a value quite unusual in the field of liquid crystals. This high quality is obviously related to the anchoring of the dense planes of the hexagonal lattice onto the flat walls of the capillary. Indeed, this anchoring is observed all along the length of the capillary over several centimeters. Therefore, the hexagonal lattice does not twist and keeps its azimuthal ϕ orientation as the capillary is scanned. In contrast, the polar "χ-scans" (Fig. 5) do not show such a good mosaic. Typical values of the χ-mosaic lie in the range 5−10° (FWHM) which could indeed be expected from the observation of the striated texture. Though these χ-mosaic values still compare quite reasonably with those reported in other previous studies, they will hamper more demanding investigations such as that of the diffuse scattering (Sect. 4).

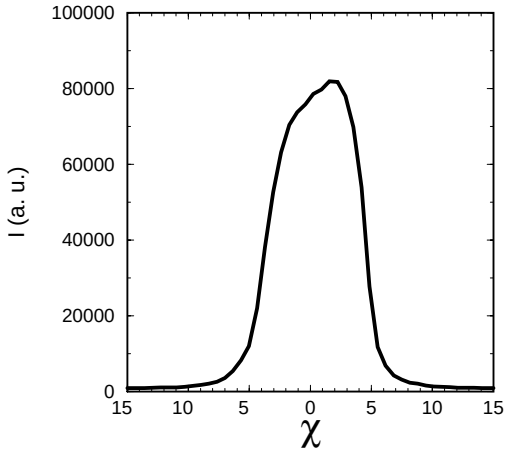

Fig. 5. X-ray scattered intensity along a χ-scan going through the (10) reflections at room temperature.

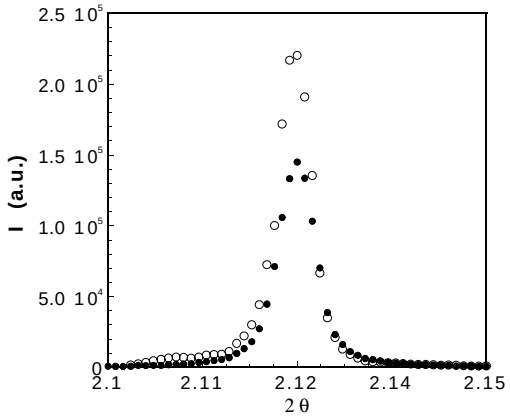

Fig. 6. X-ray scattered intensity along a 2θ-scan going through the (10) reflections (open circles) at room temperature compared to a scan of the direct beam (filled circles), which defines the experimental resolution.

Finally, the 2θ-scans going through the (10) reflections of the 2-d hexagonal lattice show a resolution limited peak (Fig. 6). This observation proves that the hexagonal lattice has true long range order. The position of the peak at $Q_{\mathrm{Bragg}} = 1.56\,\mathrm{nm}^{-1}$ gives us the value of the hexagonal lattice parameter $a = 4.64$ nm at room temperature.

4 X-ray diffuse scattering

The good crystallographic quality of our samples allows us to perform more sophisticated studies such as that of the X-ray diffuse scattering. A cross section of the reciprocal space parallel to the C_6 axis (Fig. 7) shows a (10) Bragg spot in reflection condition on one side of the image and some additional diffuse scattering on the other side. Since the sample was held fixed during the experiment and its ϕ-mosaicity ($\cong 0.1°$ FWHM) is much smaller than the scattering angle ($2\theta = 2.1°$), the additional scattering cannot be due to another (10) reflection but must arise from fluctuations. This diffuse scattering is clearly anisotropic. In order to estimate this anisotropy, we show in Figure 8 the intensity profiles along the Q_z and Q_x directions, drawn from Figure 7, for the Bragg spot (Figs. 8b, 8d) and for the diffuse scattering (Figs. 8a, 8c). The distribution of diffuse scattering is wider along the Q_z direction (a) than along the Q_x direction (c). The widths of the corresponding profiles for the Bragg spot give the contributions of both the resolution and the mosaicity. When we take these effects into account, we estimate a factor of 10 for the anisotropy of the diffuse scattering in the Oxz plane. Since the sample mosaicity ("χ-mosaic") affects the intensity profile along Q_z, this measurement does not truly correspond to the case of a single domain. Therefore, this value of 10 should only be regarded as an order of magnitude.

In contrast, we consider that the diffuse scattering intensity measured in the Oxy plane is due to a single domain, because the value of the "ϕ-mosaic" is very small and the 2θ –scans are resolution limited. Unfortunately, our sample geometry does not allow us to observe directly

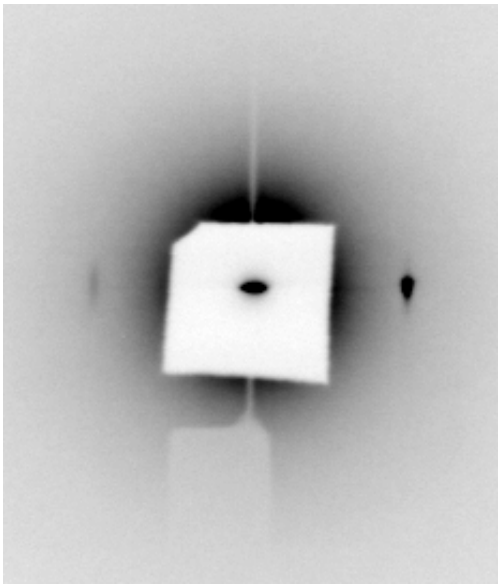

Fig. 7. 2-d image of the X-ray scattered intensity in the xOz plane. The Bragg reflection can be seen to the right of the beam-stop and the diffuse scattering signal to the left.

the Oxy reciprocal plane, because it is not possible to send the X-ray beam along the capillary axis. Nevertheless, we can perform, in this plane, different ϕ-scans at various scattering vector moduli Q (Fig. 4b) and build a complete intensity map at the vicinity of a Bragg spot (Fig. 9). The diffuse scattering intensity decreases quite rapidly as the scattering vector moves away from the Bragg condition.

In order to describe quantitatively these experimental results, we use an elastic continuum model detailed in [7c]. This model treats the fluctuations as elastic waves

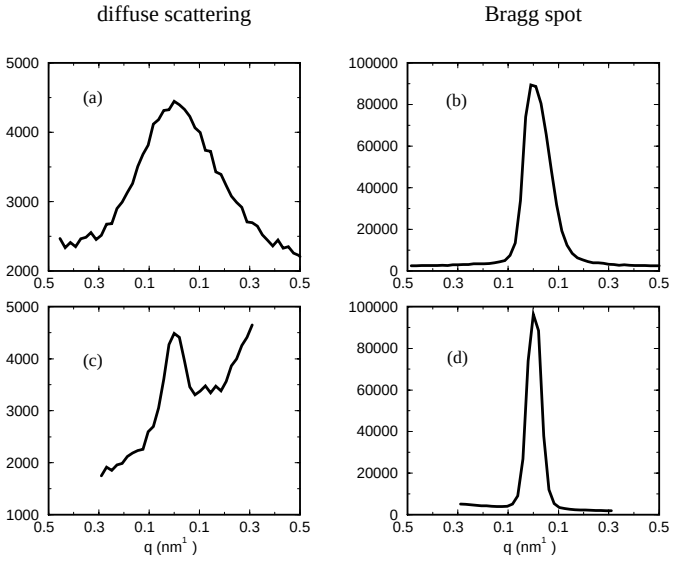

Fig. 8. Profiles derived from Figure 7 of the Bragg spot and the diffuse scattering . (a) Diffuse scattering along q_z. (b) Bragg spot along q_z. (c) Diffuse scattering along q_x. (d) Bragg spot along q_x.

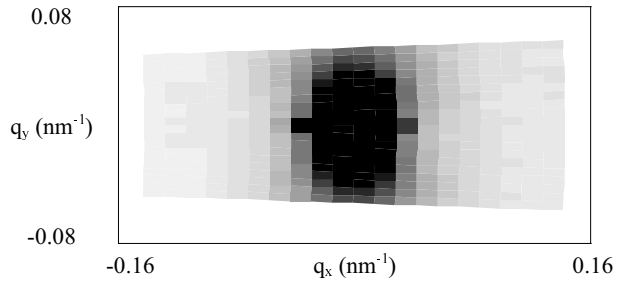

Fig. 9. Thermal diffuse scattering experimental map in the xOy plane. This map is obtained by varying the two angles 2θ and ϕ by constant increments. A linear gray scale is used to visualize clearly the distribution of the TDS.

governed by the following expression for the elastic energy density f [5,12]:

$$f = \frac{1}{2}(\lambda + 2\mu)\left(\left(\frac{\partial u}{\partial x}\right)^2 + \left(\frac{\partial v}{\partial y}\right)^2\right) + \lambda\frac{\partial u}{\partial x}\frac{\partial v}{\partial y} + \frac{1}{2}\mu\left(\frac{\partial u}{\partial y} + \frac{\partial v}{\partial x}\right)^2 + \frac{1}{2}k_3\left(\left(\frac{\partial^2 u}{\partial z^2}\right)^2 + \left(\frac{\partial^2 v}{\partial z^2}\right)^2\right)$$

where u and v are the two components of the displacement vector of an elastic wave along Ox and Oy respectively. k_3 is the Frank bend elastic constant of the columns. λ and μ are the Lamé elastic constants of the 2-dimensional hexagonal array, where $B = (\lambda + 2\mu)$ is the compressibility modulus and μ the shear modulus. It was shown [7c] that, for small $\mathbf{q}$ vectors, the diffuse scattering intensity

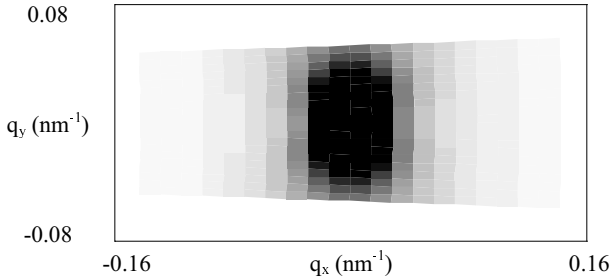

Fig. 10. Scattered intensities calculated using the elastic continuum model, with $\alpha = 3.01$, in order to fit the intensity map of Figure 9. The value of α is obtained from a linear fitting program, taking into account all the experimental points of Figure 9 (about 400 points), except a few points of very high intensities very close to the Bragg peak. The gray scales are the same in Figures 9 and 10.

at a vector $\mathbf{Q} = \mathbf{Q}_{\mathrm{Bragg}} + \mathbf{q}$ reads:

$$I(Q) = \frac{A}{q_x^2 + q_y^2}\left(\frac{\alpha(Q_{\mathrm{Bragg}}q_y)^2}{q_x^2 + q_y^2 + \alpha\Lambda_C{}^2 q_z^4} + \frac{(Q_{\mathrm{Bragg}}q_x + q_x^2 + q_y^2)^2}{q_x^2 + q_y^2 + \Lambda_C{}^2 q_z^4}\right) + C$$

where $\Lambda_C = \sqrt{\frac{k_3}{\lambda+2\mu}} = \sqrt{\frac{k_3}{B}}$ is a characteristic length of the hexagonal phase and $\alpha = \frac{\lambda+2\mu}{\mu} = \frac{B}{\mu}(2 \leq \alpha < +\infty)$. A is a constant scaling factor and C is the background correction, supposed to be constant. In the Oxy plane, this formula simply reads:

$$I(Q) = \frac{A}{(q_x^2 + q_y^2)^2}(\alpha(Q_{\mathrm{Bragg}}q_y)^2 + (Q_{\mathrm{Bragg}}q_x + q_x^2 + q_y^2)^2) + C.$$

Using this expression for the intensity, we reach a very good description of our experimental results for a value of $\alpha = 3$ (Figs. 4 and 10). This value was obtained by calculating for each experimental point the values of q_x and q_y, and then using a linear curve fitting program to determine the values of A, α and C. Both for the ϕ-scan (Fig. 4b) and the intensity map (Fig. 10), the program gives for the best fit (least mean square criterion) the same value of $\alpha = 3$ with an error bar of a few percents. Therefore, by this method, we can give a measure of $\alpha = \frac{\lambda+2\mu}{\mu} = \frac{B}{\mu}$, which characterizes the $2d$ elasticity of the hexagonal phase.

If we now come back to the diffuse scattering in the Oxz plane, the same model gives:

$$I(Q) = A\frac{(Q_{\mathrm{Bragg}} + q_x)^2}{q_x^2 + \Lambda_C{}^2 q_z^4} + C$$

which shows that the length Λ_C is the only relevant parameter in this plane. We have explained above that the distribution of scattered intensity is anisotropic by about a factor 10 and oriented along Oz. A straightforward estimation then yields the value $\Lambda_C \cong 0.2$ nm.

We have shown that the quality of our samples allows us to perform detailed diffuse scattering measurements, especially inside the Oxy plane. The continuum elastic model that we applied gives a very good description of the data and provides the value $\alpha = 3$. However, we can only estimate an order of magnitude of 0.2 nm for the characteristic length Λ_C. To conclude this section, we can compare these results to those obtained in similar previous studies of the hexagonal mesophase of thermotropic disk-like compounds [6a,7c]. Λ_C was of the same order of magnitude but the distributions of the TDS in the Oxy plane are quite different (compare for instance the ϕ-scans, Fig. 4 of [7c] to Fig. 4 in this paper). In the thermotropic hexagonal phase, the diffuse scattering extended far away from the Bragg peaks. In fact, the elastic continuum model only gives a good description of the scattering in this plane by the lyotropic hexagonal phase investigated in this paper.

5 Thermomechanical instability

5.1 Optical microscopy experiments

As mentioned in Section 3, our samples present a striated texture when observed in polarized light microscopy. This striated texture occurs frequently in hexagonal mesophases and has already been reported by numerous authors [17]. Oswald *et al.* [12] have recently studied this texture in the lyotropic mixture ($C_{12}EO_6$, H_2O) and demonstrated that it results from a thermomechanical instability by which the columns show undulations or zig-zag conformations (Fig. 14). The mechanism of the instability is the following: on cooling, the hexagonal lattice parameter decreases and since the sample dimensions are kept constant, the hexagonal lattice is dilated. This dilation can relax either by climb of transverse edge dislocations or by tilting the columns so as to increase their transverse cross-section. The first mechanism does not seem to occur in lyotropic phases so that column undulations or zig-zags are readily seen. This phenomenon is very similar to the Helfrich-Hurault effect which takes place in smectics [5]. This instability was also recently detected by NMR experiments on sheared samples [17j].

In contrast to the samples studied by Oswald *et al.* [12], the instability in our samples appears on heating. This suggests that the hexagonal lattice thermal dilation coefficient of our samples is negative, a fact that we checked by X-ray diffraction (see below). Actually, even a very small temperature jump such as that achieved by merely breathing over the sample is enough to induce this instability. The sinusoidal undulations of the columns represent the linear regime of the instability whereas the zig-zag conformations represent the non- linear regime. Due to the small wavelength ($= 5\,\mu$m at room temperature) of the instability, it is difficult to differentiate these two regimes by optical microscopy. The only typical feature that we could detect is the appearance of a slight contrast in natural light in the zig-zag regime at high temperature. This contrast probably arises from the small density difference between the bulk material and that of the domain walls located between consecutive "zig" and "zag" domains. The maximum contrast of the texture (Fig. 1) in polarized light is obtained when the capillary main axis makes an angle $\pm\,\theta$ with the polarizer-analyzer system [12] where θ is either the undulation angular amplitude or the zig-zag angle.

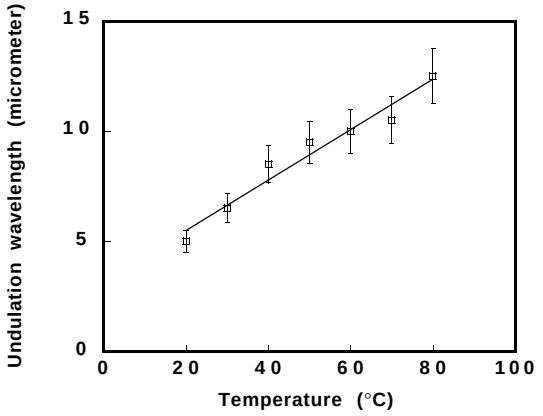

(a)

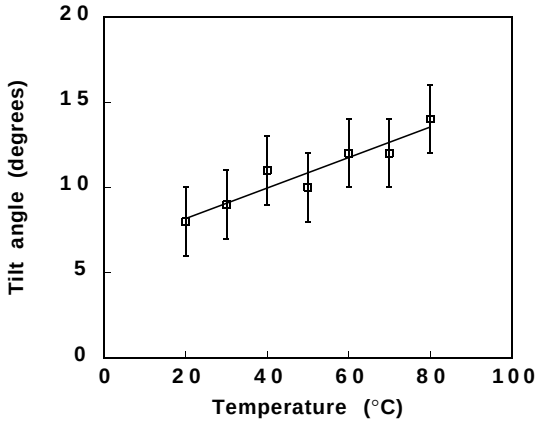

(b)

Fig. 11. (a) Wavelength Λ of the zig-zags *versus* temperature. (Error bars are estimated by taking into account the measurements dispersion over the particular sample shown in Fig. 1.) (b) Zig-zag angle θ *versus* temperature measured by the optical method developed in [12]. (Error bars essentially result from the accuracy of the determination of the maximum optical contrast.)

Both the instability wavelength, Λ and θ depend on the dilation, γ, which in turn depends on the temperature. At room temperature, the values of Λ and θ measured on our samples show a rather large dispersion compared to those carefully grown by Oswald *et al.* This is not surprising because our samples are prepared in only a few seconds and probably have a much larger defect

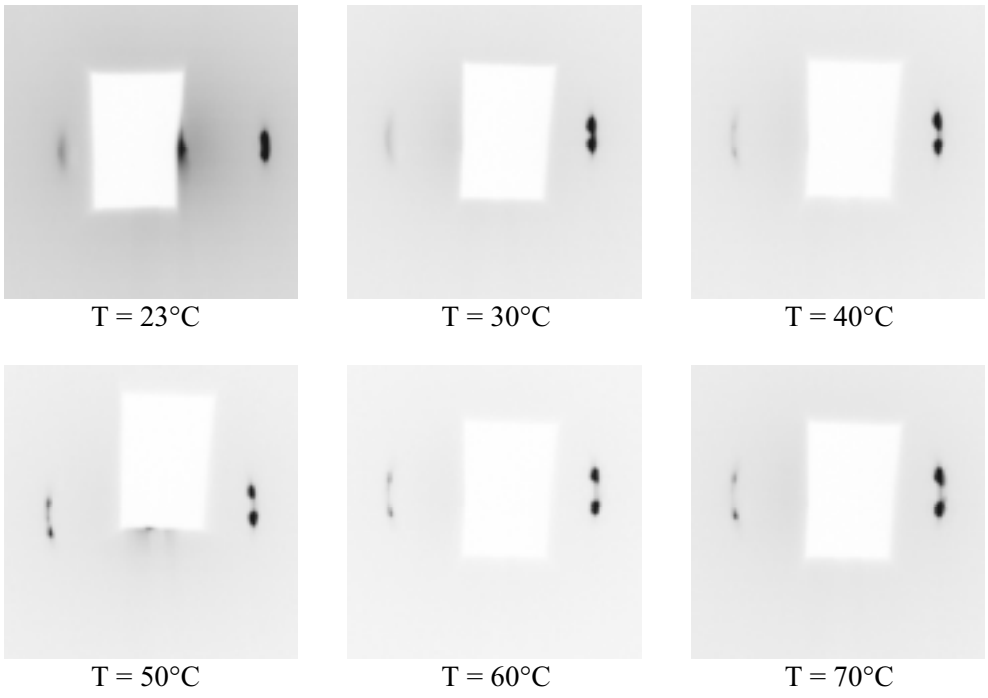

Fig. 12. Series of 2-d images of the X-ray scattered intensity in the xOz plane at different temperatures.

density. Typically, the values of θ range from 5° to 10° and those of Λ from 4 to 6 μm. These values vary from a sample to another. We measured Λ and θ as a function of temperature for a given sample using the optical methods developed by Oswald *et al.* [12] (Fig. 11). At each temperature, both Λ and θ reach their equilibrium value in a few minutes and do not evolve with time any further. θ increases regularly with temperature (heating rate: $\cong$ 1 °C/min from 20 °C to 80 °C) and therefore with dilation, in good agreement with the predictions of reference [12]. However, Λ increases by almost a factor of 3 in sharp contrast with the few % predicted by reference [12]. This discrepancy may be due to two reasons: firstly, we explore a quite larger temperature range and therefore we reach much larger dilation rates at which the model may not be valid any more. Secondly, it is possible that the behaviour of the elastic constant of compression, B, of our system differs from that of the system investigated in reference [12]. In fact, B can vary quite appreciably over the large temperature range of 50° that we have explored.

Besides, our samples are far from being defect-free. In particular, they show edge-dislocations in the system of stripes. As temperature increases and the wavelength Λ with it, these dislocations move as zippers across the sample width and suppress stripes. This phenomenon at the textural scale is similar to the climb of edge dislocations which is a classical plastic relaxation mechanism at the structural scale.

When the samples are cooled to room temperature, the optical contrast of the stripes gradually disappears, without any change of Λ until a completely aligned sample is obtained. This behaviour is observed for all cooling rates investigated, *i.e.* between 1 and 20°/min. However, the completely aligned sample is very unstable, since any slight temperature increase brings about the instability again with the wavelength of $\cong$ 5 μm usually measured at room temperature. Therefore, heating and cooling are not reversible processes but rather depend on the previous thermal history of the sample. This fact seriously hampers our quantitative analysis of this instability.

Table 1. Evolution with temperature of the sample of Figure 12. The hexagonal lattice parameter, a (nm), is measured from a 2θ-scan with the X-ray diffractometer. The zig-zag angle θ is measured from the image-plate recordings shown in Figure 12.

T (°C)	23	30	40	50	60	70
a (nm)	4.640	4.605	4.591	4.576	4.565	4.543
θ(°)	–	5.5	7	7.5	8.7	9

5.2 X-ray diffraction experiments

Table 1 clearly shows that the hexagonal lattice parameter decreases when the temperature increases, and this is the reason why the instability occurs in our samples on heating. The thermal expansion coefficient derived from Table 1 was found to be:

$$\frac{1}{a}\frac{\mathrm{d}a}{\mathrm{d}T} = -3.3 \times 10^{-4}\ ^{\circ}\mathrm{C}^{-1}.$$

This value is of the same order of magnitude as that measured on the ($C_{12}EO_6$, H_2O) system but it is of opposite sign.

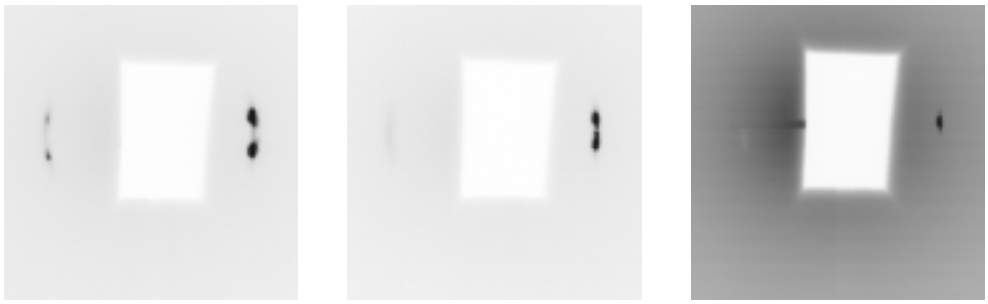

Fig. 13. 2-d images of the X-ray scattered intensity in planes parallel to Oz and: (a) at $\phi = +60°$; (b) at $\phi = -60°$; (c) at $\phi = 0°$.

A temperature ramp from room temperature to 70 °C is illustrated in Figure 12. At room temperature, one observes as expected the (10) hexagonal lattice reflection and its χ-mosaic which reaches a value of $\cong 8°$ (FWHM) is affected by the column instability. This value is to be compared with the typical values of $\theta\,(5{-}10°)$ measured by optical microscopy. As the temperature increases (heating rate $\cong 1°$/min), the (10) reflection splits into two symmetrical spots. This splitting increases with temperature to reach a maximum value of $\cong 10°$ at 70 °C. Such a splitting can be interpreted as the superposition of the two (10) reflections of the two hexagonal lattices of the "zig" and "zag" domains. The splitting is therefore the defining X-ray scattering signature of the thermomechanical instability. We have checked (Figs. 3 and 13) that the (10) reflection at $\phi = 0$ is never affected by the instability. This means that, whatever the temperature and therefore the dilation of our samples, the columns remain parallel to the flat glass plates of the capillary. This is an important point put forward by Oswald *et al.* that is proved by our X-ray scattering experiments. On cooling (cooling rate $\cong 1°$/min), the splitting decreases and finally vanishes so that the whole thermal behaviour seems qualitatively reversible, although a detailed comparison shows quantitative differences as discussed in the previous section.

At room temperature, when the tilt angle θ is small, it is actually as difficult to tell the difference between column undulations and zig-zags by X-ray scattering (see Appendix) as it is by optical microscopy. In ideal experimental conditions, (*i.e.* with no additional χ-mosaic, no instrumental broadening of any kind such as finite beam size, finite divergence, etc.) a zig-zag texture should show up on the X-ray scattering patterns by the appearance of two Bragg spots at $\chi = \pm\theta$. (A very similar phenomenon of electric-field-induced layer buckling in chiral smectic A liquid crystals was recently reported which also gave rise to a splitting of the smectic reflection observed by X-ray scattering [18].) In contrast, sinusoidal undulations should show up as a continuous distribution of scattering for $-\theta < \chi < \theta$, this distribution having peaks around $\pm\theta$. Non ideal experimental conditions will broaden the Bragg peaks of the zig-zags so that any tilt angle smaller than the angular broadening won't be detected. Similarly, the continuous distribution of scattering of the undulations will look like a broad featureless maximum of total width 2θ. Moreover, the columns being anchored along the z-axis ($\theta = 0$) at the glass surfaces, there are twist boundary layers in which the tilt varies regularly from 0 to θ [12]. The thickness of these layers decreases with increasing dilation so that at room temperature their contributions to the scattering at $\chi = 0$ may be important. Experimentally, at room temperature, we observe a broad reflection (Fig. 5) which therefore may be either due to zig-zags of small tilt angle or due to undulations. We tend to favour the undulation model for the following reasons. i) The undulations represent the linear regime valid at the onset of the instability, that is at small dilations γ. ii) The tilt angle measured optically at room temperature is at least 5°, a value that should induce a detectable splitting of the reflection in the case of zig-zags. iii) We have not observed any contrast due to domain walls in natural light by optical microscopy at room temperature. However, the quality of our samples does not really allow us to reach a definitive answer to this question. Nevertheless, at high temperature, the scattered intensity at $\chi = 0$ falls down to the background level which clearly indicates that the non-linear zig-zag regime prevails.

6 Conclusion

We have described a very simple, useful and cheap method for producing highly aligned samples of a hexagonal liquid-crystalline phase, suitable for detailed X-ray analysis. Preliminary experiments show that this method also efficiently applies to the hexagonal phase of other materials such as non-ionic surfactants ($C_{12}EO_6$, H_2O) and diblock copolymers. We are therefore confident that this simple technique will prove useful to investigate very different systems. The production of a highly aligned sample allowed us to record the thermal diffuse scattering intensity. Its good description by a simple elastic continuum model provided estimates of the characteristic mechanical parameters of the mesophase ($\alpha = 3$ and $\Lambda_C \cong 0.2$ nm) in agreement with other estimates previously derived from X-ray scattering studies and analysis of textures. However, for this lyotropic phase, the distribution of the TDS in the hexagonal plane is highly localized close to the Bragg

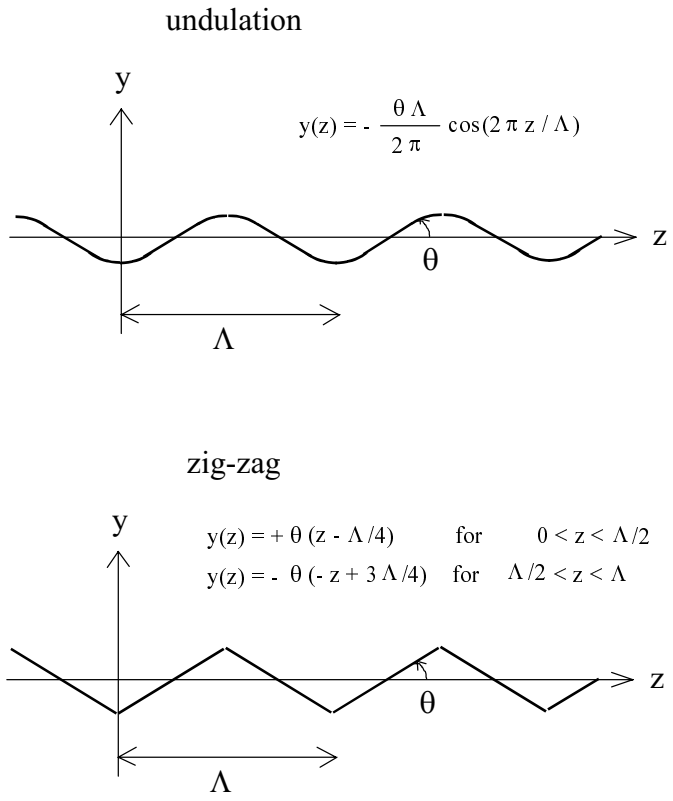

Fig. 14. Profiles $y(z)$ of the molecular columns for the two models. For the undulation model, the profile is taken as a cosine wave. The two parameters, Λ and θ define the amplitude along the Oy direction.

peaks, a result in sharp contrast to thermotropic hexagonal phases for which the TDS extended far away from the reflections. We presently do not understand the origin of such a variation between the two kinds of materials. Clearly, the study of other hexagonal mesophases is required to try to solve this question and we hope that this aligned domain growth technique will prove useful to achieve this task. Finally, we completely confirm the analysis of the thermomechanical instability presented by Oswald *et al.* [12]. Moreover, we have detected the X-ray signature of the instability in the fully developed, non-linear regime as a splitting of four of the six hexagonal Bragg peaks and demonstrated that the instability remains confined in the plane parallel to the flat glass plates of the capillary. It should be here noted that the appearance of this striated texture, when it is uniform over a large distance, indicates that the sample observed is highly aligned.

We are deeply indebted to J.C. Geminard, P. Oswald, J. Prost, L. Sallen and J. Selinger for pleasant and enlightening discussions. J.F. Berar, M. Gailhanou and S. Lefebvre are warmly thanked for taking part in the synchrotron X-ray scattering experiments at LURE and ESRF. We are also grateful to S.H.J. Idziak and C.R. Safinya for drawing our attention to this particularly interesting lyotropic system.

Appendix: Undulation or zigzag?

Two models are proposed for the striated texture (Fig. 14):

- Undulations of infinite columns following a sinusoidal profile, with a maximum angular amplitude θ.
- The so-called "zigzag" configuration resulting from the periodic stacking of tilted "zig" and "zag" domains, at the angles θ and $-\theta$, with walls between two adjacent domains.

A χ-scan of a Bragg peak (at $\phi = 60°$ or $\phi = -60°$) is directly related to the bulk distribution of the tilt-angle of the columns inside the sample. In order to try to discriminate between the undulation and the zigzag models, we will calculate in this appendix the intensity profile of a χ-scan for both models.

We assume that the undulation or the zigzag is located in the Oyz plane and we approximate a χ-scan to a scan along the Oz direction. For both models, all the columns have the same profile $y(z)$, which is periodic along z with a period Λ. Since the tilt angle is small, we can identify $\mathrm{d}y/\mathrm{d}z$ to the tilt angle at a given point of the profile. The intensity of a χ-scan reads:

$$i(\chi) = (1/\Lambda) \int_0^{\Lambda} \delta(\chi - \mathrm{d}y/\mathrm{d}z)\mathrm{d}\chi.$$

The expressions of $i(\chi)$ for the two models are:
– Zigzag model:

$$i^{z-z}(\chi) = \frac{1}{2}(\delta(\chi - \theta) + \delta(\chi + \theta)).$$

– Undulation model:

$$i^{\mathrm{und}}(\chi) = \frac{1}{\pi\sqrt{\theta^2 - \chi^2}} \text{ for } |\chi| < \theta \text{ and}$$
$$i^{\mathrm{und}}(\chi) = 0 \text{ for } |\chi| \geq \theta$$

$i^{z-z}(\chi)$ and $i^{\mathrm{und}}(\chi)$ both have singularities at $\chi = \theta$ and $\chi = -\theta$. Since the experimental χ-scans show wide peaks of several degrees (FWHM), then we have to consider a superposition of undulations or zigzags rather than the ideal situation depicted in Figure 14. We can consider different origins for this superposition.

First, we consider the influence of the mosaicity, assuming that the sample is made of several domains, slightly disoriented around the z direction, and describing this disorientation by a Gaussian distribution $f(\chi)$: in this case, we assume that the maximum tilt angle θ is the same for all the domains.

The total intensity is the convolution product of $i(\chi)$ by the Gaussian distribution $f(\chi)$:

$$I_{\mathrm{mos}}(\chi) = \int_{-\infty}^{+\infty} i(X) f(\chi - X)\mathrm{d}X \quad \text{with}$$
$$f(\chi) = \frac{1}{\sqrt{2\pi}\sigma} \exp\left(-\frac{\chi^2}{2\sigma^2}\right).$$

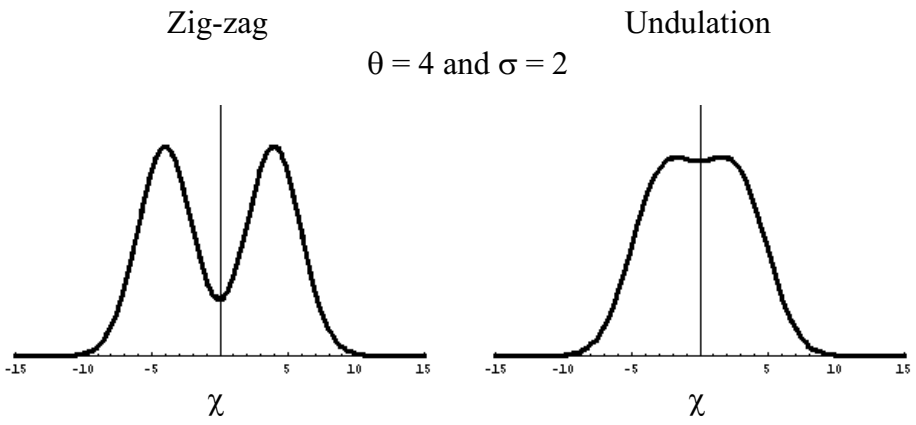

Fig. 15. Simulated χ-scans calculated in the frame of the zig-zag and undulation models for $\theta = 4$ and $\sigma = 2$. The undulation model is the only one able to reproduce the shape of the experimental χ-scan of Figure 5.

We could also consider the influence of other factors such as a distribution $P(\theta)$ of the maximum tilt angle θ around an average value for instance. In this case, the calculations lead to results that are quite similar to those derived above by studying the influence of mosaicity, so we will only take the mosaicity distribution into account.

We obtain the two following expressions:

– For the zig-zag model:

$$I^{z-z}(\chi) = \frac{1}{2\sqrt{2\pi}\sigma} \times \left(\exp\left(-\frac{(\chi-\theta)^2}{2\sigma^2} \right) + \exp\left(-\frac{(\chi+\theta)^2}{2\sigma^2} \right) \right).$$

– For the undulation model:

$$I^{\mathrm{und}}(\chi) = \int_{-\theta}^{+\theta} \frac{1}{\pi\sqrt{\theta^2 - X^2}} \frac{1}{\sqrt{2\pi}\sigma} \exp\left(-\frac{(\chi - X)^2}{2\sigma^2} \right) \mathrm{d}X.$$

This last expression is numerically evaluated using the MATHEMATICA 3.0 software, for different combinations of the two parameters θ and σ.

Figure 15 shows numerical simulations using the above two expressions for the experimental χ-scan of Figure 5. The width of this experimental profile is 8° (FWHM). On the one hand, the value of θ cannot be larger than 4° because otherwise the total width of the profile would be larger than 8°. On the other hand, we never measured by optical microscopy a value of θ smaller than 4°. So we choose $\theta = 4°$ for the simulation. Then, we examine the influence of the second parameter σ. For the zig-zag model, one obtains either a splitted profile (Fig. 15) or, by increasing the value of σ, a single large peak of width much larger than 8° however. For the undulation model, the value $\sigma = 2$ provides a good description of the experimental profile. Values of σ larger than 2 increase the total width of the profile without changing its shape. For values of σ smaller than 2, the shape of the profile is slightly modified, with a decrease of the intensity around $\chi = 0$.

To conclude, we see that the undulation model is the only one which can reproduce the global shape of the χ-scan of Figure 5. Although both models are strongly idealized, this nevertheless suggests that the instability is better described in terms of undulations at room temperature.

References

1. A.M. Levelut, J. Chim. Phys. **80**, 409 (1983).
2. A. Skoulios, Adv. Liq. Crystals **1**, 169 (1975).
3. G. Ungar, Polymer **34**, 2050 (1993).
4. Y. Hendrikx, A.M. Levelut, Mol. Cryst. Liq. Cryst. **165**, 233 (1988).
5. P.-G. De Gennes, J. Prost, *The Physics of Liquid Crystals* (Clarendon, Oxford, 1993).
6. (a) A.M. Levelut, J. Phys. Lett. **40**, L81 (1979); (b) M. Ebert, R. Kleppinger, M. Soliman, M. Wolf, J.H. Wendorff, G. Lattermann, G. Staufer, Liq. Cryst. **7**, 553 (1990); (c) H. Guterman, Z. Luz, E.J. Wachtel, R. Poupko, J. Charvolin, Liq. Cryst. **7**, 335 (1990); (d) J. Malthête, P. Davidson, Bull. Soc. Chim. Fr. **131**, 812 (1994); (e) H. Fischer, S.S. Ghosh, P.A. Heiney, N.C. Maliszewskyj, T. Plesnivy, H. Ringsdorf, M. Seitz, Angew. Cheva. Int. Ed. Engl. **34**, 795 (1995); (f) P. Sakya, J.M. Seddon, R.H. Templer, R.J. Mirhin, G.J.T. Tiddy, Langmuir **13**, 3706 (1997).
7. (a) C.R. Safinya, K.S. Liang, W.A. Varady, N.A. Clark, G. Andersson, Phys. Rev. Lett. **53**, 1172 (1984); (b) E. Fontes, P.A. Heiney, M. Ohba, J.N. Haseltine, A.B. III Smith, Phys. Rev. A **37**, 1329 (1988); (c) P. Davidson, M. Clerc, S.S. Ghosh, N.C. Maliszewskyj, P.A. Heiney, J. Hynes Jr, A.B. III Smith, J. Phys. II France **5**, 249 (1995).
8. I. Koltover, S.H.J. Idziak, P. Davidson, Y. Li, C.R. Safinya, M. Ruths, S. Steinberg, J.N. Israelachvili, J. Phys. II France **6**, 893 (1996).
9. (a) I.W. Hamley, K.A. Koppi, J.H. Rosedale, F.S. Bates, K. Almdal, K. Mortensen, Macromolec. **26**, 5959 (1993); (b) F.A. Morrison, J.W. Mays, M. Muthukumar, A.I. Nakatani, C.C. Han, Macromolec. **26**, 5271 (1993); (c) F.S. Bates, K.A. Koppi, M. Tirrell, K. Almdal, K. Mortensen, Macromolec. **27**, 5934 (1994); (d) N.P. Balsara, H.J. Dai, P.K. Kesani, B.A. Gorretz, B. Hammouda, Macromolec.

27, 7406 (1994); (e) G. Schmidt, S. Müller, P. Lindner, C. Schmidt, W. Richtering, J. Phys. Chem. B **102**, 507 (1998).
10. (a) M. Gharbia, M. Cagnon, G. Durand, J. Phys. Lett. **46**, L683 (1985); (b) M. Cagnon, M. Gharbia, G. Durand, Phys. Rev. Lett. **53**, 938 (1984); (c) M. Gharbia, T. Othman, A. Gharbi, C. Destrade, G. Durand, Phys. Rev. Lett. **68**, 2031 (1992).
11. L. Sallen, P. Oswald, J.C. Géminard, J. Malthête, J. Phys. II France **5**, 937 (1995).
12. P. Oswald, J.C. Géminard, L. Lejcek, L. Sallen, J. Phys. II France **6**, 281 (1996).
13. (a) D. Roux, A.M. Bellocq, in *Physics of Amphiphiles: micelles, vesicles and microemulsions*, edited by V. Degiorgio, M. Corti (North Holland, Amsterdam, 1985); (b) C.R. Safinya, D. Roux, G.S. Smith, S.K. Sinha, P. Dimon, N.A. Clark, A.M. Bellocq, Phys. Rev. Lett. **57**, 2718 (1986).
14. S. Deudé, Ph.D. thesis, University of Paris-Sud, Orsay (to be published).
15. (a) M. Bessière, G. Bessenay, J. Frouin, M. Jouvin, S. Lefebvre, Nucl. Instrum. Methods A **261**, 591 (1987); (b) E. Elkaïm, S Lefebvre, R. Kahn, J.F. Bérar, M. Lemmonier, M. Bessière, Rev. Sci. Instrum. **63**, 988 (1992).
16. (a) J.P. Simon, E. Geissler, A.M. Hecht, F. Bley, F. Livet, M. Roth, J.L. Ferrer, E. Fanchon, C. Cohen-Addad, J.C. Thierry, Rev. Sci. Instrum. **63**, 1051 (1992); (b) J.F. Bérar, J.P. Simon, J.L. Ferrer, D. Dallé, Materials Science Forum **228-231**, 223 (1996).
17. (a) C.A. Gilchrist, J. Rogers, G. Steel, E.G. Vaal, P.A. Windsor, J. Colloïd Interf. Sci. **25**, 409 (1967); (b) F.B. Rosevear, J. Soc. Cosmetic Chemists **19**, 581 (1968); (c) J. Rogers, P.A. Windsor, J. Colloïd Interf. Sci. **30**, 500 (1969); (d) B. Lühmann, H. Finkelmann, G. Rehage, Makromol. Chem. **186**, 1059 (1985); (e) F. Livolant, Y. Bouligand, J. Phys. **47**, 1813 (1986); (f) F. Livolant, A. Leforestier, Mol. Cryst. Liq. Cryst. **215**, 47 (1992); (g) D. Durand, J. Doucet, F. Livolant, J. Phys. II France **2**, 1769 (1992); (h) Y. Hendrikx, B. Pansu, J. Phys. II France **6**, 33 (1996); (i) L. Ramos, P. Fabre, Langmuir **13**, 682 (1997); (j) S. Müller, P. Fisher, C. Schmidt, J. Phys. II France **7**, 421 (1997).
18. R.E. Geer, S.J. Singer, J.V. Selinger, B.R. Ratna, R. Shashidhar, Phys. Rev. E **57**, 3059 (1998).